

X-Ray Crystal Spectroscopy of Sub-picosecond Laser-Produced Plasmas beyond 50 keV

G. Hölzer,^{*1} E. Förster,^{*} M. Grätz,[†] C. Tillman,[†] and S. Svanberg[†]

**Max-Planck-Arbeitsgruppe "Röntgenoptik" an der Friedrich-Schiller-Universität Jena, Max-Wien-Platz 1, D-07743 Jena, Germany; and †Department of Physics, Lund Institute of Technology, P.O. Box 118, S-221 00 Lund, Sweden*

Received October 15, 1996; revised February 10, 1997

The interaction of a sub-picosecond (sub-ps) laser with a high-Z target produces a hard x-ray continuum, but to our knowledge no high-resolution study of the line emission is known. We present here crystal spectroscopy as a tool for the observation of energetic line x-radiation from a sub-ps laser-produced plasma. Reflection properties of flat and bent crystals for x-ray spectroscopy are analyzed theoretically for both the Bragg and the Laue geometries and optimized for a crystal spectroscopy of hard (>50 keV) x-radiation. The crystal setup is optimized for spectroscopic applications with regard to high throughput and spectral resolution. The characteristic tantalum $K\alpha, \beta$ - and $L\alpha, \beta$ -line emissions from a sub-ps laser-produced plasma is observed for the first time. A resolving power of about 450 is achieved which is much higher than that for comparable absorption filter techniques ($E/\Delta E \approx 15$). © 1997 Academic Press

1. INTRODUCTION

With the availability of high-power lasers with ultra-short pulse durations it has, during the last few years, become possible to generate hard x-rays by focusing the laser radiation on targets with high atomic number Z . In 1992 Kmetec *et al.* (1) demonstrated that radiation with energies extending up into the MeV range can be obtained by using a 10 Hz Ti:sapphire laser system. This system reached the TW power level in 100 fs pulses by employing the chirped-pulse-amplification technology.

Hard x-rays from laser-produced plasmas have several potential applications for inner-shell spectroscopy (2) and for medical/biological applications, e.g. magnification radiography (3), scatter-reduced imaging (4), and element-specific differential imaging of contrast agents (5). The differential imaging technique is based on the use of two images, exposed with x-ray radiation both above and below the K -edge of the contrast agent, which can be subtracted to enhance the contrast in the parts of the image containing the contrast agent. Differential imaging for coronary angiography has already been tested with synchrotron x-radiation, using iodine (K -edge at 33.2 keV) as a contrast agent (6, 7). Gadolinium (K -edge at 50.2 keV) is another clinically approved contrast agent where Gd $K\alpha$ - and Ta $K\alpha$ -radiation from a laser-produced source can be used for the double exposure, above and below the K -edge of Gd.

¹ E-mail: ghoelzer@roentgen.physik.uni-jena.de.

However, in order to develop these and other applications, it is necessary to characterize the emission spectrum of the laser-based x-ray source. Reliable spectroscopy is needed for the optimization of the useful radiation from the source for the given applications. In particular, it is desirable to enhance the characteristic line emission in relation to the Bremsstrahlung continuum for differential imaging applications (5).

The measurement of ultrashort, extremely bright x-ray pulses causes severe problems. A standard technique to measure the spectral distribution of an x-ray source is to use energy-dispersive detectors, such as NaI scintillators or semiconductor detectors. These single-photon counting detector systems allow direct multichannel display of the x-ray spectrum. Unfortunately, these powerful detectors are hampered by pile-up problems. These are caused by the simultaneous arrival of many quanta in the ultrashort and ultra-intense x-ray bursts. The incoming flux must be heavily attenuated and the recording of a spectrum of moderate quality will therefore take at least on the order of 1 h for a 10-Hz system.

An alternate measurement technique is to observe the transmission through an array of elements with increasing atomic number, for which the K -absorption edges move in a systematic way (8, 9); however, the resolution is rather limited because of the finite number of elements. Combinations of ionization chambers, scintillation detectors, and CCD cameras with different absorption filters are also used as diagnostic tools for the emitted x-rays (1, 10). The spectral resolving power ($E/\Delta E$) is about 2–5 (10), which is far from the value of about 50 required to separate the Ta $K\alpha$ -doublet. Recently a higher resolution observation of the Ta $K\alpha$ -emission from a femtosecond-laser plasma source was reported using an optimized filter technique with K -edges near the Ta $K\alpha$ -doublet in combination with absolutely calibrated detectors, reaching a spectral resolving power of about 15 (10).

A further technique uses standard CCD-arrays, operated in the single-photon counting mode (11). In this mode every pixel acts as an energy-dispersive detector and is consequently sensitive to pileup problems. However, a large number of x-ray photons can be registered simultaneously due to the huge amount of available pixels. Unfortunately, these devices are hampered by their poor sensitivity at higher photon energies due to an absorber (silicon) thickness of only a few micrometers. The spectral resolving power is of the order of 30.

Crystal spectroscopy can provide a much higher resolving power than the above-mentioned energy-dispersive and filter methods. Furthermore, crystal spectroscopy is not limited by high-flux problems. Techniques for crystal spectroscopy of continuous sources in the Bragg and Laue geometries are described in Siegbahn (12), for example. Crystals in the Bragg geometry are extensively used for the characterization of emission spectra of pulsed laser plasma sources in the energy range from 1 to 10 keV (1.2 to 0.12 nm). Two-dimensionally bent crystals for high-resolution spectroscopy (13) and quasi-monochromatic imaging of the emitting source (14) allow extensive characterization of the spectral and spatial emission characteristics of the plasma.

To our knowledge, no crystal spectroscopic investigations for photon energies above 50 keV exist for femtosecond-laser-driven x-ray sources. We use high-resolution crystal spectroscopy for the study of our laser-produced x-ray source in the energy range above 50 keV. Results presented in this study are obtained from the characteristic tantalum K -emission at $E \geq 56$ keV. A high resolving power ($E/\Delta E \approx 450$) allows

the separation of the characteristic Ta $K\alpha$ lines from the Bremsstrahlung continuum and the resolution of the doublet structure. The absolute resolution, $\Delta E \approx 125$ eV, corresponds to one tenth of the distance between the Ta $K\alpha$ doublet lines. The yield of characteristic radiation, which is an important parameter in differential imaging, could be determined from the measured spectra.

General considerations involved in the optimal selection of crystals for use in the high energy x-ray spectroscopy (>50 keV) are presented in Section 2. The experimental setup of both the laser-produced plasma source and the crystal spectrometer is shown in Section 3. The results of the measurements are presented in Section 4, and finally, the results are discussed in Section 5.

2. REFLECTION PROPERTIES OF CRYSTALS IN THE HIGH-ENERGY RANGE

To our knowledge, published data for crystal spectroscopy of ultra-short pulse laser-produced plasmas is only available for the energy region below 12 keV. We present results of high-resolution measurements for considerably harder radiation which motivates a discussion of characteristic crystal reflection properties for these high energies ($E > 50$ keV). Theoretical data presented in this article are calculated taking into account the experimental conditions, i.e., measurements of the Ta $K\alpha$ doublet ($E_{\text{Ta } K\alpha 1} = 57.532$ keV, $E_{\text{Ta } K\alpha 2} = 56.277$ keV) excited by a sub-ps laser plasma source. The crystal setup for the experiment has to be optimized for a high throughput because the average intensity of the ultrashort x-ray pulses is low. The source is small (<60 μm) and can thus be approximated by a point source.

2.1. Crystal Structure and the Intensity of Crystal Reflections

The structure of the crystals is assumed to be ‘‘perfect’’, i.e. the reflection properties can be described theoretically by the dynamical theory of x-ray diffraction for flat and bent crystals (15, 16). In this way the reflection properties of the real crystals can be calculated with a high degree of precision and this is important for a precise quantitative correction of measured spectra. Additionally, the reflection properties of perfect crystals are homogeneous over the entire crystal. To fulfill these requirements, the quality of the crystal has to be tested experimentally by topographic (projection and plane wave topography (17)) and diffraction techniques (see for example (18)) and imperfect crystals are thereby eliminated. The experience shows that the reflection properties of crystals like silicon, germanium and quartz are usually perfect within the above mentioned sense. Nevertheless, each crystal specimen should be analyzed by routine examinations before and especially after the bending process.

A high throughput of the crystal is highly desired considering the low average x-ray flux of the pulsed source. The selection of the optimal crystal orientation, i.e. crystal cut is essential because the reflection properties of crystals are not isotropic. Generally the intensity of crystal reflections (identified by the Miller indices hkl) is determined by the crystal structure and can be characterized by the structure factor F_{hkl} :

$$F_{hkl} = \sum_{j=1}^N f_j e^{-2\pi i(hx_j + ky_j + lz_j)} \quad [1]$$

TABLE 1

Reflection Parameters (Structure Factor, Bragg Angle, and Crystal Limited Resolving Power) for the Most Intense Reflections (and Selected Higher Orders of the Reflections 112 and 115) of Silicon and Germanium Assuming Ta $K\alpha_1$ -Radiation

hkl	n	Si (Z = 14)			Ge (Z = 32)		
		F_{hkl}	Θ_B [°]	$(E/\Delta E)_{RC}$	F_{hkl}	Θ_B [°]	$(E/\Delta E)_{RC}$
220	2	67.1	3.2	9000	176.7	3.1	3500
111	1	58.0	2.0	3900	150.6	1.9	1600
400	4	56.5	4.6	20000	141.0	4.4	9000
224	2	48.8	5.6	>20000	115.5	5.3	16000
113	1	44.1	3.8	19000	114.2	3.6	7600
440	4	42.6	7.9	>20000	96.2	6.2	>20000
133	1	37.8	5.0	>20000	92.3	4.8	16000
026	2	37.3	7.2	>20000	81.1	6.9	>20000
333	3	32.8	5.9	>20000	76.2	5.7	>20000
444	4	32.9	7.9	>20000	69.0	7.6	>20000
115	1	32.8	5.9	>20000	76.1	5.7	>20000
660	6	23.2	9.7	>20000	44.5	9.3	>20000
224	2	48.8	5.6	>20000	115.5	5.3	16000
448	4	17.2	11.2	>20000	30.3	10.8	>20000
6612	6	6.1	16.9	>20000	6.8	16.3	>20000
8816	8	2.4	22.9	>20000	1.1	21.9	>20000
115	1	32.8	5.9	>20000	76.1	5.7	>20000
3315	3	3.6	18.0	>20000	3.6	17.3	>20000
4420	4	2.0	24.3	>20000	0.7	23.3	>20000

The Fourier sum is over all N atoms (characterized by their individual atomic scattering factor f_j and the coordinates x_j , y_j , and z_j) of the unit cell of the crystal. In Table 1 the calculated structure factors F_{hkl} of the most intense reflections (and some selected higher orders for the reflections 112 and 115) for silicon and germanium are shown. It has to be mentioned that the number of observable reflections for these two crystals is further limited (see Table 1) due to the cubic crystal symmetry of silicon and germanium. Quartz is intentionally not included in any further investigations due to the small structure factors. The largest structure factor of quartz is 38 for the reflection $10\bar{1}1$.

The data in Table 1 are calculated for Ta $K\alpha_1$ -radiation. The structure factor is only slightly energy-dependent due to small energy-dependent corrections for the atomic scattering factors f_j for energies distant from the energies of the absorption edges of silicon and germanium. Therefore F_{hkl} can be used for the comparison of the relative intensity from different reflections taking into account the crystal structure only.

The Bragg angle θ_B for a selected x-ray energy can be calculated using the well-known Bragg equation

$$n \cdot \lambda = 2d \sin \theta_B, \quad [2]$$

with n being the reflection order, d the lattice plane distance, and λ the x-ray wavelength. A preselection of appropriate intense reflections for a high throughput of the x-ray spectrometer is possible, taking into account the structure factor. The corresponding Bragg angle is important for the geometric setup. Two characteristic features are important in the hard x-ray region:

- The Bragg angles encountered are small; for Ta $K\alpha_1$ they are usually smaller than 6° for the most intensive reflections of silicon and germanium (see Table 1). In the Laue case small Bragg angles require a deliberate limitation of the horizontal divergence of the incoming x-ray beam to prevent an overlap of the incoming and diffracted beams. The horizontal divergence $\Delta\theta_{\text{hor}}$ of the incoming beam has at least to be restricted to $\Delta\theta_{\text{hor}} < 2\theta_{\text{B}}$. This condition limits the available spectral range to $\Delta E = E\Delta\theta_{\text{hor}}/\tan\theta_{\text{B}}$ and the registration of a large spectral range requires several exposures.

- The interaction of ultra-short laser pulses with high- Z target generates continuum x-radiation up to the MeV range. Consequently, the intensity contributed by the ‘‘harmonics’’ of the x-ray emission line energy E observed at the same Bragg angle, i.e., from $2E, 3E, \dots$, due to high-order crystal reflections ($n = 2, 3, \dots$) has to be taken into account. For example, Ta $K\alpha_1$ ($E = 57$ keV) is observed in the reflection 220 using a silicon crystal ($F_{hkl} = 67.1$). At the same Bragg angle intensity contributions from the high-order reflections 440 (for $E = 114$ keV, $F_{hkl} = 42.6$) and 660 (for $E = 171$ keV, $F_{hkl} = 23.2$) are registered. In a first approximation these intensity contributions are proportional to the structure factor (for perfect crystals) and it is obvious that their sum can be considerable if the photon flux is intense in the high-energy range.

2.2. Integrated Reflectivity of Flat Crystals

The integrated reflectivity R_{int} is a quantitative measure of the ‘‘throughput’’ of the crystal, i.e., the luminosity of the spectrometer. It takes into account not only the crystal structure (see Sect. 2.1), but also the actual diffraction geometry, i.e. the Bragg (reflection) or the Laue (transmission) geometry. R_{int} can be easily determined for perfect crystals (like silicon and germanium) using the dynamical theory of x-ray diffraction (15, 16). The reflection curve of the selected crystal reflection is calculated, followed by an integration of the reflection curve along the angular scale.

A simple approximation of the achievable resolving power of the crystal $(E/\Delta E)_{\text{RC}}$ can be obtained from the Bragg equation:

$$\left(\frac{E}{\Delta E}\right)_{\text{RC}} = \frac{\tan\theta_{\text{B}}}{\Delta\theta_{\text{RC}}}. \quad [3]$$

Calculated results are presented in Table 1. Generally Eq. [3] represents only a dispersion relation connecting the angular width of the reflection curve $\Delta\theta_{\text{RC}}$ to the corresponding energy width. The calculated resolving power represents an upper limit determined only by the reflection of a ‘‘perfect’’ crystal. This value decreases due to geometric aberrations, the finite resolution of the detector and

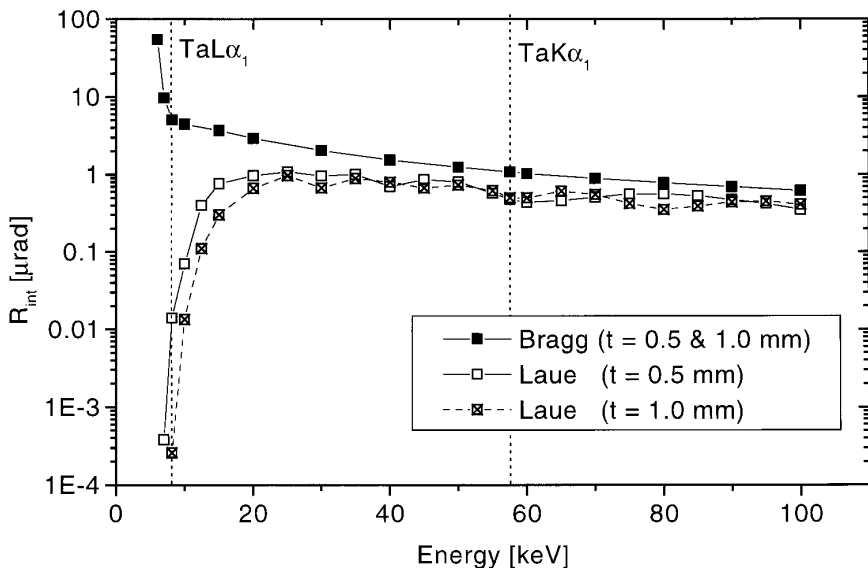


FIG. 1. Integrated reflectivity of silicon (reflection 115) as a function of x-ray energy for the Bragg and the Laue case. The parameter t is the crystal thickness.

other instrumental factors. It has to be calculated for the actual spectrometer setup and ray-tracing codes (see for example (19)) must be used taking into account the realistic reflection curve shape.

Typical results for the energy dependence of the integrated reflectivity in the hard x-ray region are shown in Fig. 1. The data is calculated for silicon (reflection 115) from 5 to 100 keV including the Ta $L\alpha_1$ - and Ta $K\alpha_1$ -emission lines, which are marked in the figure. The results allow the following general conclusions:

- The integrated reflectivity R_{int} decreases continuously for hard radiation. Discontinuities in R_{int} exist near absorption edges of the crystal atoms.
- Characteristic differences exist between the Bragg and the Laue case.

In the Laue case R_{int} decreases significantly at low energies, due to the high photoelectric absorption of the crystal in this energy range. The intensity reduction is more pronounced for thicker crystals, so that the crystal thickness has to be taken into account explicitly for the calculation of the integrated reflectivity in the Laue case. A characteristic of the Laue case are also obvious oscillations (see Fig. 1) in the $R_{\text{int}}(E)$ dependence due to the superposition of x-rays scattered at frontside and at the backside of the crystal. In contrast to the Laue case, a distinct increase of R_{int} at low energies can be observed in the Bragg case, where R_{int} for Ta $L\alpha_1$ is about ten times larger than for Ta $K\alpha_1$ (see Fig. 1). In the Bragg case the incoming wave is heavily attenuated by extinction. The x-ray extinction depth is much smaller than the absorption depth (4.2 μm and 1.5 mm, respectively for Si 115 and Ta $K\alpha_1$ -radiation). Therefore no explicit dependence of R_{int} on the thickness exists if the crystals are

thicker than 2–3 times the extinction depth. This holds for most of the relevant crystal thicknesses from several 100 μm to several mm.

- The integrated reflectivity in the Bragg case is always equal to or larger than in the Laue case, assuming all other diffraction conditions are the same. The difference is much larger at lower energies: for Ta $K\alpha_1$ the ratio of the integrated reflectivity of the Bragg to the Laue case is about two, and for Ta $L\alpha_1$ this ratio is about 10^4 (silicon, reflection 115, thickness 1 mm; see Fig. 1). For the Laue case the integrated reflectivity can be slightly increased by the use of thinner crystals, but for these thin crystal slices problems with the crystal mounting can occur. The flatness of the crystal will be distorted by stresses due to the mounting or by uncontrolled bending of the crystal plate simply due to its own weight.

Silicon (atomic number $Z = 14$) and germanium ($Z = 32$) are the most common crystals for applications in x-ray spectroscopy with a high degree of crystal perfection and intense reflections. Their reflection properties are compared in the Bragg and Laue geometries (Figs. 2a, 2b). Reflection 115 is selected and the data for the Laue case is calculated assuming a crystal thickness of 1 mm.

- In the Bragg case, R_{int} for germanium is usually a factor of two larger than the corresponding values for silicon crystals (for Ta $K\alpha_1$ 2.21 μrad and 1.08 μrad , respectively). This is mainly a consequence of the higher structure factor for germanium (see Table 1); the integrated reflectivity is approximately proportional to F_{hkl} for perfect crystals. Moreover, the effect of the K -absorption edge of Ge at about 11.1 keV upon R_{int} is visible with a steep decrease of R_{int} near this absorption edge.

- In the Laue case the situation is completely reversed, the germanium crystal is nearly opaque for energies below 20 keV due to the high photoelectric absorption. In the energy range to 50 keV the integrated reflectivity of germanium in the Laue case is considerably lower than for silicon. Assuming Ta $K\alpha_1$ -radiation, the integrated reflectivities of silicon and germanium are nearly equal. Only for very high energies $E > 70$ keV the higher structure factor of germanium starts to dominate the absorption and the R_{int} of germanium is slightly higher than for silicon.

In conclusion, germanium and silicon show characteristic differences in their reflection properties. Germanium provides a higher reflectivity than silicon for the Bragg case due to higher structure factors, although silicon can be the better choice for the Laue case due to its considerably lower photoelectric absorption.

2.3. Spectrometer “Throughput” Enhancement with Bent Crystals in Focusing Geometries

Focusing geometries with bent crystals are standard techniques to achieve a higher luminosity of the spectrometer by an increased aperture and an increased integrated reflectivity of the bent crystal and/or to prevent a decrease in the spectrometer resolution caused by source size broadening. The reflection properties of bent crystals have to be calculated using the dynamical theory of x-ray diffraction in elastically deformed crystals (see for example (16)). The deformation of a bent crystal is described by the deformation vector \mathbf{u} . The effective deformation for the x-ray diffraction at a selected lattice plane is

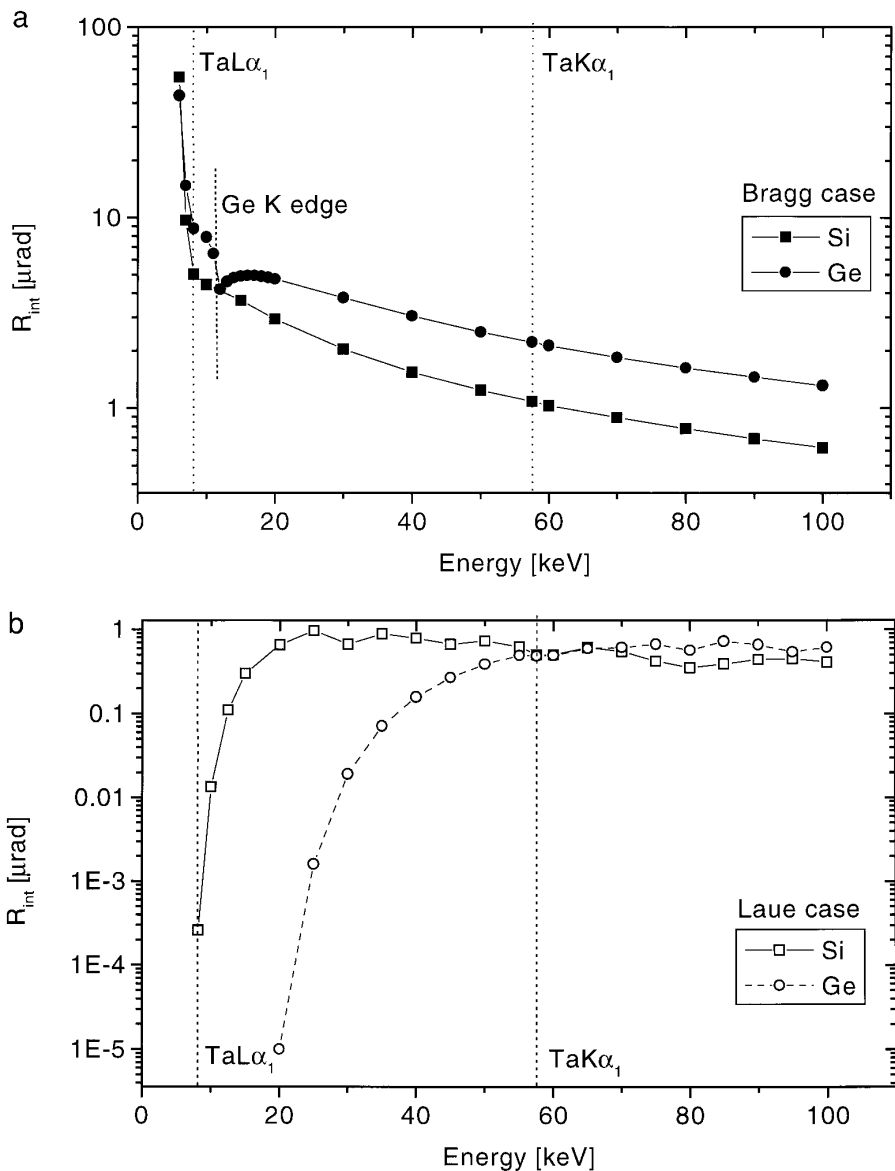


FIG. 2. Comparison of the integrated reflectivities of silicon and germanium (reflection 115) as a function of x-ray energy for the Bragg (a) and the Laue (b) case.

defined by the scalar product of \mathbf{u} and the diffraction vector \mathbf{h} which is perpendicular to the lattice planes. This value of the scalar product is different in the Bragg and Laue case, and the effect of the crystal deformation onto the shape of the reflection curve and the integrated reflectivity is correspondingly different in both cases. The following considerations for bent crystals are deliberately restricted to cylindrically bent crystals (a

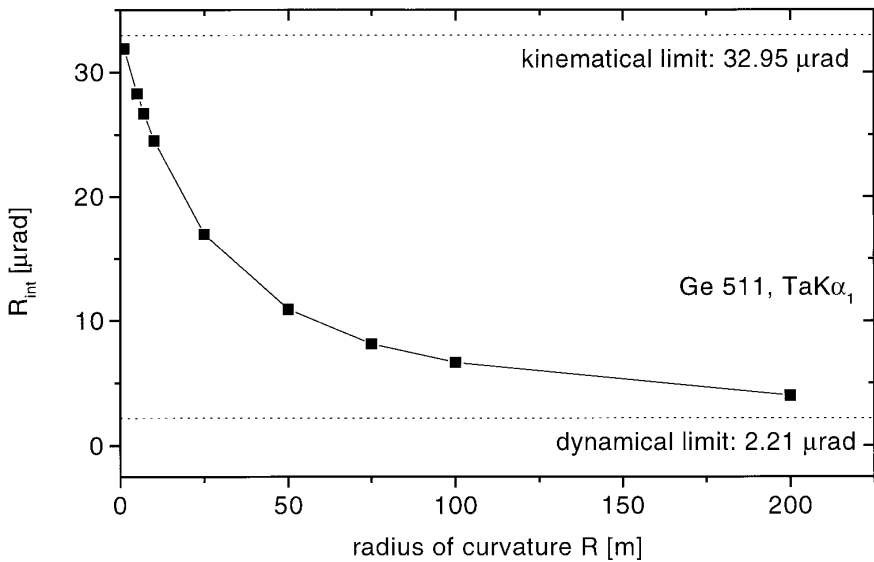


FIG. 3. Integrated reflectivity of a cylindrically bent germanium crystal as a function of the bending radii.

standard shape in x-ray spectroscopy) and to symmetrical x-ray diffraction, for reasons of simplicity. The results can easily be generalized for doubly bent crystals and asymmetric x-ray diffraction.

2.3.1. Bragg case. In the symmetrical Bragg case the effective deformation gradient C for the x-ray diffraction is proportional to

$$C \sim \frac{\partial^2(\mathbf{h} \cdot \mathbf{u})}{\partial s_o \partial s_h} \sim \frac{1}{R} \left(\cos^2 \theta_B - \frac{\sigma}{1 - \sigma} \sin^2 \theta_B \right) \quad [4]$$

with \mathbf{s}_o and \mathbf{s}_h as the directions of the incoming and diffracted beam, respectively (see (16)). R is the radius of curvature and σ the Poisson ratio of the crystal. The first term takes into account the pure geometric curvature of the lattice planes. It is the dominant factor for the diffraction of hard x-rays, where Bragg angles are typically small. The second term takes into account the depth change of the lattice plane spacing due to the elastic deformation of the crystal. In an isotropic approximation this effect can be described using the Poisson ratio σ (16). It becomes significant only for large Bragg angles near 90° .

A simple model for the effect of bending upon the diffraction properties can be found in (20). As a result of the increased bending the interference conditions for the wave attenuation become more and more disturbed and the penetration depth of the x-radiation grows from the perfect-crystal limit to the absorption-limited value (for example for Ta $K\alpha_1$, germanium, reflection 115 from $2 \mu\text{m}$ to $46 \mu\text{m}$). Correspondingly, the integrated reflectivity increases from the perfect crystal limit of 2.2

μrad to the kinematical limit of $32.9 \mu\text{rad}$, i.e. the luminosity of the spectrometer can be increased considerably by means of bending (Fig. 3). This intensity gain is achieved by a broadening and an asymmetric shape of the reflection curve (Fig. 4). The FWHM of the reflection curve increases from 0.4 arcsec for a flat crystal to 5.7 arcsec for a cylindrically bent crystal with a moderate radius of curvature of 10 m . Due to the increasing asymmetry the width of the curve cannot be precisely characterized by its FWHM. The width at $1/10$ of the peak reflectivity is a better approximation of the width of the reflection curve and should be used for the calculation of the resolving power according to Eq. [3].

The use of germanium crystals was already favored for the Bragg case, according to the conclusions in Section 2.2. This choice has to be emphasized for hard x-radiation by a comparison of the reflection curves of bent silicon and germanium crystals (reflection 115, cylindrical curvature with $R = 10 \text{ m}$) in Fig. 5. Due to the smaller absorption coefficient a much larger broadening of the reflection curve, i.e. a drastic loss of the resolving power, can be observed for silicon. The large asymmetry of the reflection curve can cause a significant asymmetric deformation of the spectral line shape if the width of the asymmetric reflection curve is comparable with, or larger than, the spectral line width. A precise determination of the spectral line position is difficult under these conditions.

Focusing spectrometers using bent crystal schemes in the Bragg case, e.g. Johann, Johansson and von Hamos geometries (see for example (21) as a review) are standard tools in x-ray plasma spectroscopy within the energy range from 1 to 10 keV (1.2 to 0.12 nm).

2.3.2. Laue case. In the symmetrical Laue case the deformation vector $\mathbf{u}(z)$ is perpendicular to \mathbf{h} , assuming isotropic elastic properties of the crystals (16). Therefore the scalar product is zero and the reflection properties correspond to those of a flat crystal. However, theoretical and experimental investigations (22) show significant deviations in the reflection properties, if the existing anisotropy of the elastic properties of the crystals is taken into account.

Asymmetric Laue geometries ($\mathbf{h} \cdot \mathbf{u} \neq 0$) have to be applied for an intentional enhancement of the spectrometer luminosity. Reflection curves can be calculated using the model of Erola (23) or, if the absorption in the crystal can be neglected for hard x-radiation (or neutrons) by the model of Albertini (24). Typical reflection curves of bent crystals in the Laue case are broadened, but in contrast to the Bragg case they preserve their symmetric shape (23, 24).

Standard setups for focusing spectrometers using the Laue scheme are the Cauchois and the DuMond geometries which are used for spectroscopy of hard x- and γ -rays (25). To our knowledge, no application of the Laue case to x-ray plasma diagnostics has been reported.

2.4. Conclusions for the Experimental Observation of the Tantalum Line Emission

The TaL emission spectra can be observed at energies of about 9 keV . In this region the integrated reflectivity of crystals in the Bragg case is considerably higher than in the Laue case (see Figs. 2a, 2b) and a standard flat crystal spectrometer is selected.

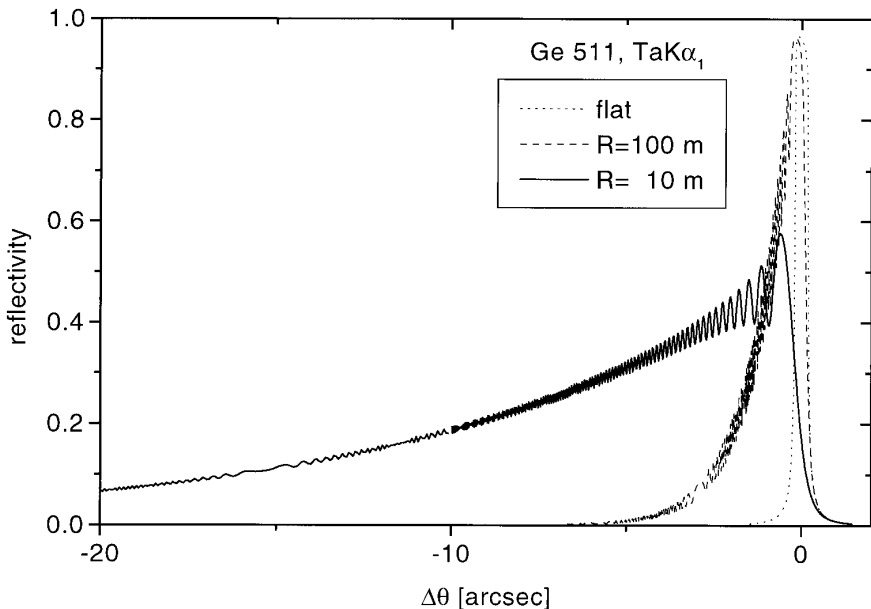


FIG. 4. Calculated reflection curves for flat and cylindrically bent germanium crystals with bending radii $R = 100$ m and $R = 10$ m.

For the observation of the Ta K emission at about 60 keV the Bragg case also has the advantage of the relatively higher luminosity. For example in the Laue case using the most intense reflection 224 of a flat silicon crystal (thickness 1 mm) an integrated reflectivity of $0.8 \mu\text{rad}$ (37 times lower than that in the Bragg case) can be achieved. But the absolute value of the integrated reflectivity of the crystals is considerably smaller than for the Ta L emission and should be enhanced by bending the crystal, for example.

The resolving power of bent crystals has to be carefully checked for the real experimental conditions and the broadening of the reflection curve has to be taken into account. A germanium crystal (reflection 115 to guarantee small contributions from high-energetic harmonics) with a cylindrical curvature of 3.1 m provides a high integrated reflectivity ($29.7 \mu\text{rad}$). The FWHM of the asymmetric reflection curve is 14.5 arcsec. The resolving power is calculated according to Eq. [3] neglecting other instrumental broadening effects than the crystal itself. A value $(E/\Delta E)_{\text{RC}}$ of about 440 is determined using the full width at 1/10 of the maximum reflectivity (about 50 arcsec) to take into account the asymmetric reflection curve shape. The value fully satisfies our experimental requirements. Consequently a cylindrically bent germanium crystal in a Bragg geometry is suitable also for a high-resolution and high-luminosity spectroscopy of the Ta $K\alpha$ -doublet, i.e. in the hard x-ray region.

3. EXPERIMENTAL SETUP

A terawatt laser system (26) based on chirped-pulse amplification was used for x-ray generation. The laser system typically delivered output pulses with a wavelength

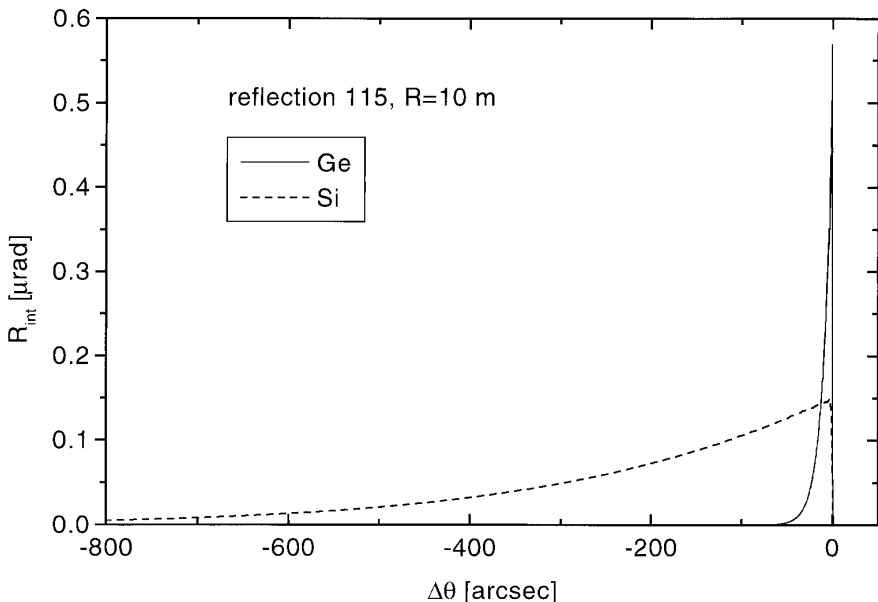


FIG. 5. Comparison of the reflection curves of cylindrically bent ($R = 10$ m) silicon and germanium crystals.

of 792 nm at a duration of 150 fs (FWHM) with energies of 150 mJ onto the radiation target. The laser pulses were directed into a vacuum chamber with a residual air pressure of about 20 hPa and focused onto a metallic target with an off-axis $f/1$, gold-coated mirror (see Fig. 6). This results in peak intensities on the target of about 10^{18} W/cm². Tantalum foils (250 μm thick) were used as targets. The target was rotating and mechanically stabilized with respect to the laser focus, in order to reduce fluctuations in x-ray intensity and to stabilize the absolute position of the source ($\pm 3\mu\text{m}$). The vacuum chamber was shielded with 5 cm lead bricks, both for safety reasons and for a reduction of scattered x-rays.

The x-ray emission is characterized by its very short time duration of the order of 5 ps and a small x-ray source size ($< 60\mu\text{m}$). The spectral emission is described by characteristic line emission from the target element and a Bremsstrahlung-like continuum. This continuum extends from soft x-rays (< 1 keV) up to the MeV region. The x-ray peak intensity after filtering with 0.15 mm Cu (10% transmission at 25 keV) is of the order of 100 MW/srad. This corresponds to a flux of approximately 10^{10} photons/srad/pulse assuming an average photon energy of 60 keV.

The spectrometer setup is presented in Fig. 7. Experimentally characterized perfect crystals of silicon (flat, surface orientations 111 and 110, thickness 900 μm) and germanium (flat and cylindrically bent, surface orientation 115, thickness 1 mm) were used. The crystals and the reflection geometries were optimized for a high integrated reflectivity according to the theoretical considerations in Section 2 (see Table 1). The germanium crystal has a triangular shape (height 25 mm, length 100 mm) to minimize anticlastic effects, i.e. a deviation from an exact cylindrical shape caused by the elastic

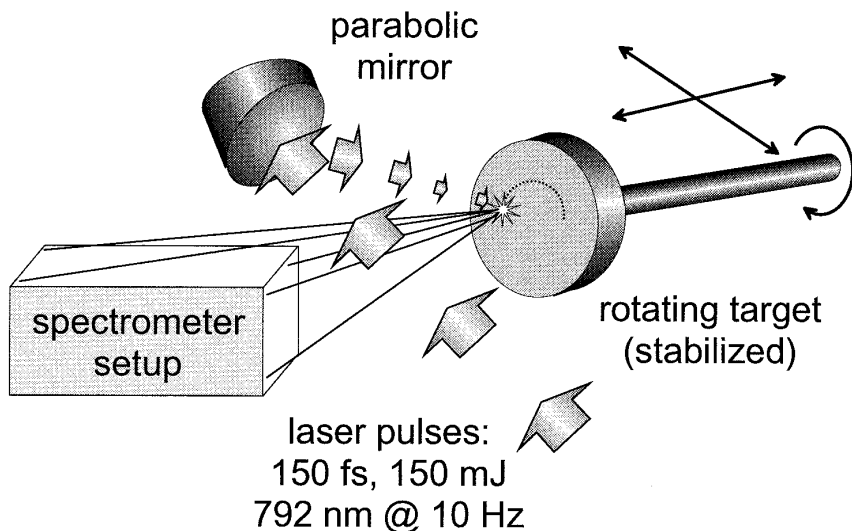


FIG. 6. X-ray generation setup with the mirror and the target placed inside a vacuum chamber.

deformation of the crystal. The adjustable bending device is described in (27). The precision and the homogeneity of the bent crystal shape were checked by optical and x-ray methods over a length of 50 mm along the crystal length. The radius of curvature could be fixed with a precision of $\Delta R/R = 0.6\%$. Small systematic deviations from the cylindrical shape were observed, pointing to a parabolic shape of the bent crystal. The deviations between the assumed cylindrical and the actual shape were small (< 1 arcmin over a distance of 50 mm).

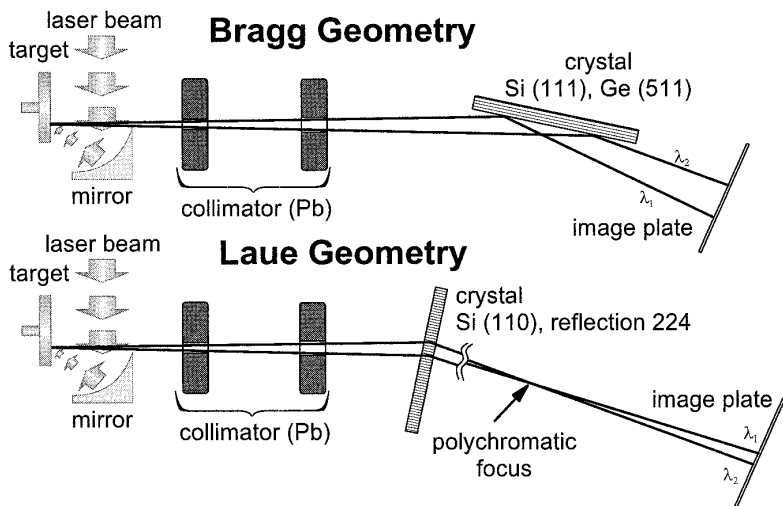


FIG. 7. Overview of the spectrometer setup in Bragg and Laue geometries.

TABLE 2

Crystal and Reflection Parameters for the Observation of Ta $K\alpha$ and Ta $L\alpha$ Radiation

Emission line	Crystal (surface orientation)	Geometry	Reflection	Θ_B [°]	R_{int} [μ rad]
Ta $K\alpha_1$ (57.532 keV)	Ge (115)	Bragg	115	5.68	2.2
	Si (110)	Laue (thickness 1 mm)	224	5.58	0.8
Ta $L\alpha_1$ (8.146 keV)	Si (111)	Bragg	111	14.05	36.7

A crucial point for the experiment was the shielding of scattered radiation to ensure a high signal-to-noise ratio and a strong suppression of the background. Two lead bricks (thickness 4 cm) with cylindrical holes were used to limit the aperture to about 2° .

Two different imaging detector systems were used for the recording of the spectra: Photo-stimulable luminescent image plates (Fuji BAS-III) or a customized imaging system consisting of a fiber-optic scintillator plate in direct contact with an intensified CCD system. The image plate offers the advantage of excellent linearity over 4–5 orders of magnitude combined with a high sensitivity (100 \times better than photographic x-ray film) (28). The current readout configuration limits the resolution to 200 μ m. The fiber-optic scintillator plate (thickness 5 mm) consists of terbium-doped optical fibers (LKH-6, Collimated Holes, Inc.), arranged in a hexagonal grid with 15 μ m center-to-center spacing. The scintillation light is guided through the fiber plate with the spatial information being conserved. This allows for a thick scintillator plate and thereby stronger absorption even at high energies (29). The scintillator is directly coupled to an image intensifier (MCPI40, Photek) and viewed by a CCD system (STAR I, Photometrics). The overall resolution is 55 μ m and is limited by the CCD pixel size in the current configuration. The CCD based system offers a direct and fast readout after exposure, whereas the image plates have to undergo a more time-consuming readout and erasure cycle. The overall sensitivity of the CCD system at 60 keV is approximately a factor of 2 lower than for the image plate. The dynamic range is 1:4000. An improved optical coupling between the intensifier and the CCD is expected to increase the sensitivity by two orders of magnitude.

4. MEASUREMENTS AND RESULTS

The goal of the experiments is the verification of the characteristic K- and L-line emission spectra which are produced due to the interaction of ultra-short laser pulses with a tantalum target. The Ta $L\alpha, \beta$ line spectrum was recorded in an experiment with a silicon crystal (reflection 111) in a symmetric Bragg case. Parameters for the experiments are shown in Table 2. A large energy range extending from 8 to 10 keV must be covered for the measurement of the entire spectrum. The entire spectral range had to be registered onto the image plate using different Bragg angles in two separate exposures, because of the small aperture. The results are presented in Fig. 8. Figs. 8a

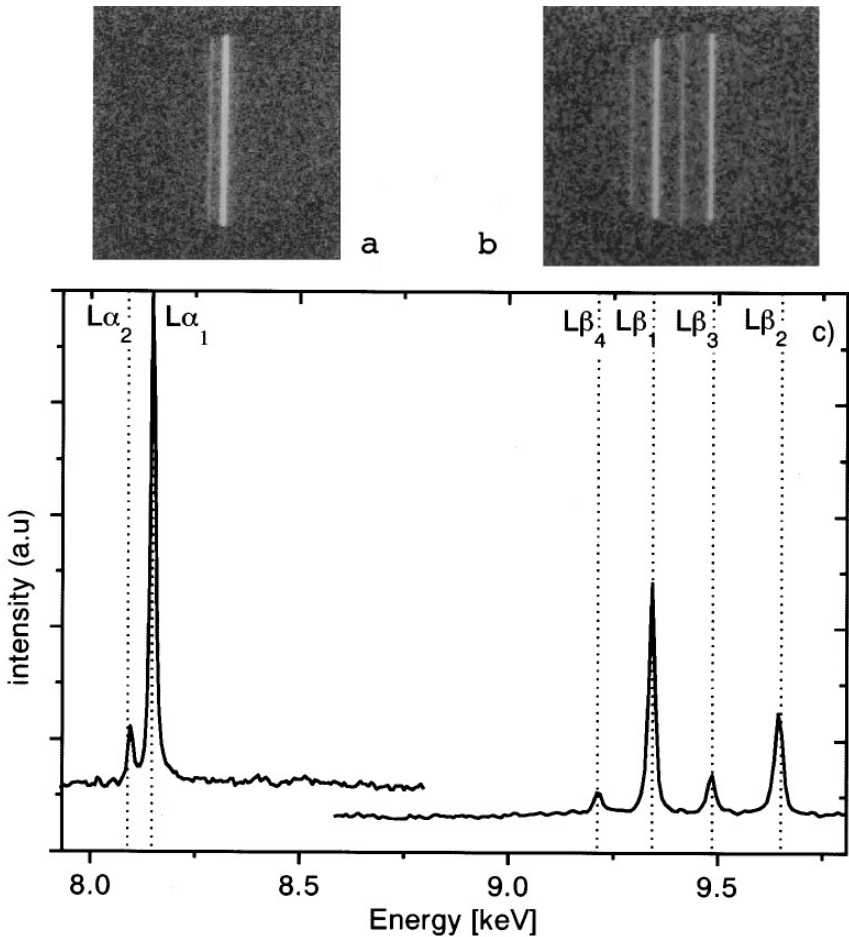


FIG. 8. Image plate pictures (a, b) and intensity profiles (c) for the Ta $L\alpha,\beta$ emission spectrum exposed in two different exposures (Bragg case, silicon, reflection 111). The positions of the emission lines for the solid state (according to Bearden (30)) are marked by dashed lines using the positions of Ta $L\alpha_1$ and Ta $L\beta_1$ as references.

and 8b show pictures of the Ta $L\alpha$ and Ta $L\beta$ spectra from the image plate; Fig. 8c shows the corresponding intensity profile. The two strongest lines ($L\alpha_1$ and $L\beta_1$) were used for energy calibration. The positions of the other L-lines were in agreement with tabulated spectral data for solid state spectra (30). Theoretically, the integrated intensities of $L\alpha_1$ and $L\beta_1$ should be nearly equal because of the same exposure conditions, but the experimental values differ by a factor of about two. The average x-ray flux in the experiments is low and in our experiments usually 6000–9000 shots are necessary for an exposure of the image plate, i.e. an exposure time of 10 to 15 min. The experimentally observed difference between the two exposures is the result of significant fluctuations in the primary x-ray flux, i.e. between the single shots.

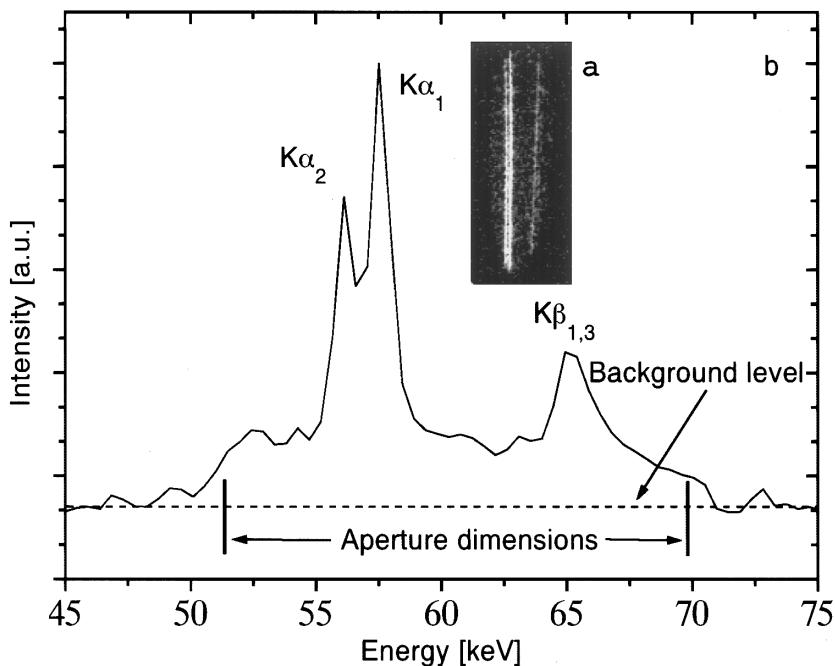


FIG. 9. Image plate picture (a) and intensity profile (b) of the Ta $K\alpha,\beta$ spectrum in the Laue geometry (silicon, reflection 224).

Monitoring of the primary x-ray flux from the source within the limited spectral range around the observed line spectrum is imperative for a quantitative analysis of relative line intensities using different exposures.

Ta $K\alpha$ -radiation was recorded in both the Bragg and the Laue cases. A silicon crystal in the reflection 224 was used in the symmetric Laue case and the results are shown in Fig. 9. The source to crystal distance was about 440 mm, the distance crystal-image plate was 680 mm. An exceptionally high x-ray flux during one experimental campaign allowed the registration of this spectrum despite the low integrated reflectivity in the Laue case (see Section 2.4). The spectrum even includes the weak Ta $K\beta$ -line, its intensity being about 1/3 of Ta $K\alpha_1$. The limiting aperture of the lead bricks is clearly visible on the exposed images and allows a separation of the general background of the image plate from the continuum part of the x-ray spectrum inside of the aperture window. From these measurements it is possible to determine the ratio of characteristic to continuum radiation. Assuming a linear background due to the continuum inside the aperture window, Ta $K\alpha_1$, Ta $K\alpha_2$, and Ta $K\beta_{1,3}$ were fitted with a Lorentzian for each line, which is characterized by three variable parameters: the position, the FWHM and the intensity at the maximum. The integrated intensities of each line were determined. The results show that the ratio of characteristic line emission to continuum emission is nearly 1:1 as for the region of the Ta $K\alpha$ -doublet (from 52 to 62 keV) as for the entire spectral range between Ta $K\alpha$ and Ta $K\beta_{1,3}$ (from 52 to 70 keV).

A deformation of the circular aperture to an elliptical shape is visible in Fig. 9a. If the image plate was set at the position of the polychromatic line focus in the Laue case, i.e. with the distance from the crystal to the polychromatic focus being the same as the distance from the source to the crystal, this ellipse would fully degenerate to a vertical line. A slit at the position of the polychromatic focus can be used for an effective suppression of scattered radiation.

A germanium crystal was used for the experiment in the Bragg case, taking advantage of the higher integrated reflectivity of germanium (see Section 2). The reflection 115 was chosen to suppress contributions from high-order reflections from the continuum part of the spectrum. The triangularly shaped crystal was mounted on an adjustable bending device (see (27)) and was used both flat and cylindrically bent (radius of curvature 3.1 m). The distance source-crystal was 320 mm. The distance crystal-image plate was 1280 mm both for the flat and for the bent crystal experiments. The images and the corresponding intensity profiles are presented in Fig. 10.

For the flat germanium crystal the FWHM of the reflection curve is very narrow (0.3 arcsec) for Ta $K\alpha_1$. The resolution is therefore limited by the spatial resolution of the image plate (200 μm). The latter corresponds to an angular resolution of about 26 arcsec (for a source-detector distance of 1600 mm), which is by a factor of 100 larger than the angular width of the reflection curve. The intensity of the Ta $K\alpha$ -doublet is weak and the Ta $K\alpha_2$ -emission line is too weak to be observed (see Fig. 10a).

A higher integrated reflectivity can be achieved by cylindrically bending the crystal in order to increase the width of its reflection curve to fit the lower spatial resolution of the detector. Theoretical calculations (see Section 2) show that a bending radius of 3.1 m increases the integrated reflectivity by a factor of 10 as compared with the flat crystal. The luminosity gain due to bending is clearly visible in the image (Fig. 10b) and the intensity profile (Fig. 10c) of the experimental observations. The spectral lines are slightly broadened due to the lower resolution of the bent crystal, but the doublet lines are nevertheless clearly separated. The intensity gain is about 10 as expected by the theoretical calculations.

First results using the scintillator imaging system in combination with a bent crystal in Bragg geometry (Ge, reflection 115, $R = 6.2$ m) were obtained and are shown in Fig. 11. The source-crystal distance was 320 mm, the crystal-scintillator distance was 700 mm. The exposure time was the same as for the image plates. The intensity profile shows well resolved Ta $K\alpha$ - and Ta $K\beta$ -lines. The main advantage of this system is the improved resolution, which is about four times better than for the image plate, and the much faster readout procedure.

5. CONCLUSIONS

Criteria for an optimum selection of crystals for high resolution spectroscopy in the hard (>50 keV) x-ray range are presented. Examples illustrate characteristic changes of the reflection properties of crystals in the range between 5 and 100 keV and the influence of crystal bending onto these properties. According to our results silicon and germanium crystals are well suited for a high resolution spectroscopy in this high-energy range due to their high crystal symmetry, ‘‘perfect’’ real structure

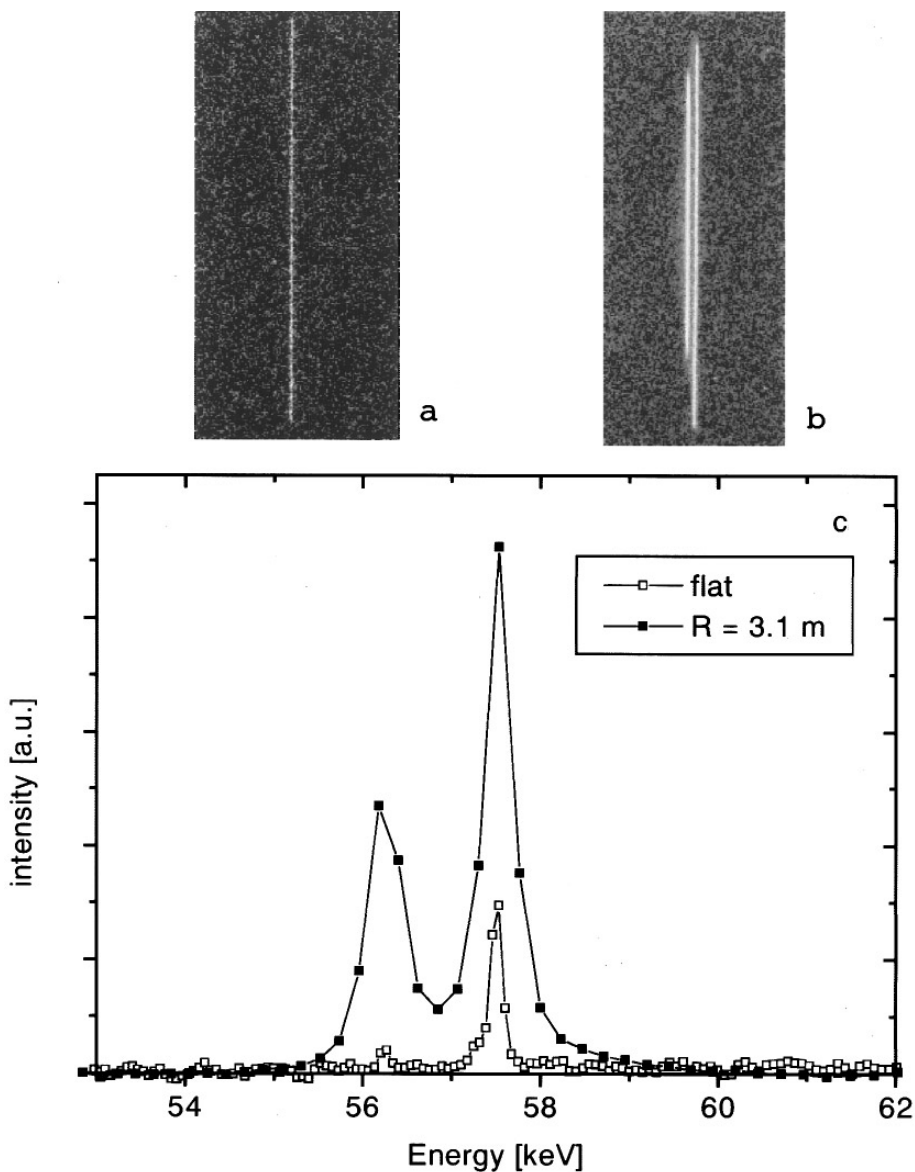


FIG. 10. Image plate pictures (flat crystal (a), cylindrically bent crystal (b)) and intensity profiles (c) of the Ta $K\alpha$ -doublet in the Bragg geometry (germanium, reflection 115).

and large integrated reflectivity. The spectrometer throughput can be further increased by using bent crystal geometries.

Germanium ($Z = 32$) has significant advantages in the Bragg case because of its larger integrated reflectivity and considerably smaller broadening of the reflection curve upon bending. It is, however, unsuitable for the Laue (transmission) case due

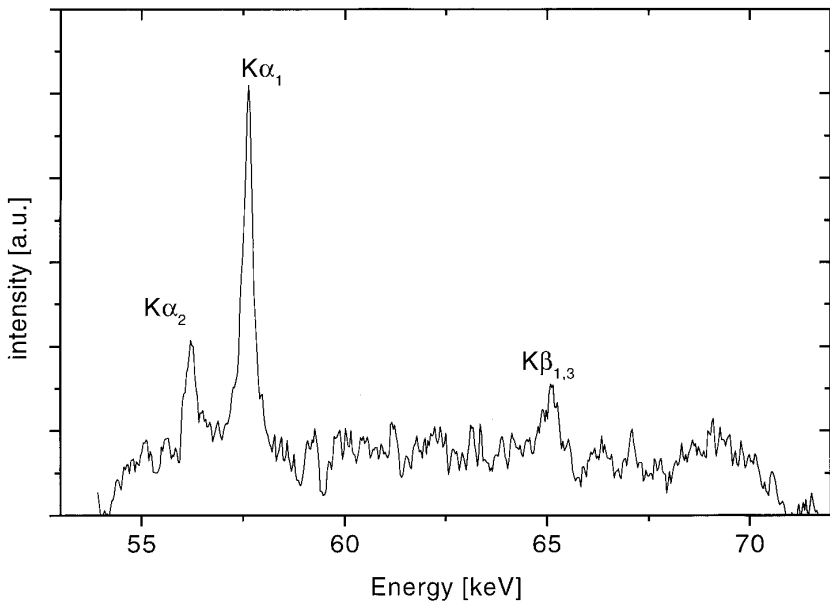


FIG. 11. Intensity profile of the Ta $K\alpha$ -doublet in the Bragg geometry (germanium, reflection 115, cylindrically bent with $R = 3.1$ m) obtained with the scintillator/CCD system.

to a high photoelectric absorption for energies lower than 50 keV. Silicon ($Z = 14$) has a lower integrated reflectivity in the Bragg case than germanium. But in the Laue case the integrated reflectivity is higher due to its low photoelectric absorption. The theoretical considerations show that the application of a cylindrically bent germanium crystal in the Bragg case is an optimal choice for the observation of hard Ta $K\alpha$ -radiation (about 57 keV). It provides a high integrated reflectivity, which is essential for the spectroscopy of short-pulsed x-ray sources. At the same time the resolving power of this crystal setup is high enough to resolve the Ta $K\alpha$ -doublet structure.

Results of high-resolution observations of the characteristic $K\alpha, \beta$ - and $L\alpha, \beta$ - line emission spectra of tantalum were reported obtained with a sub-ps laser-produced plasma, for the first time to our knowledge. The spectral resolution is nearly 125 eV, corresponding to a resolving power of 450, which is much better than comparable results with single-photon counting energy-dispersive detectors. Furthermore, the exposure time using the crystal spectrometer can be much shorter compared to energy-dispersive measurements, because of the absence of the pile-up problem. The observed spectral line positions correspond to solid-state spectral data (30). No emission lines from highly ionized tantalum were found in the experiments.

In conclusion, crystal spectrometers in Bragg and Laue cases are demonstrated as working tools in the high energy and high peak but low average intensity range, which is characteristic for sub-ps laser-produced x-radiation. Quantitative high-resolution measurements of the characteristic emission spectra are possible. Special attention in the experiments has to be paid to the shielding of the primary beam (due to small Bragg angles) and the high background due to scattering of the hard continuum

radiation. The spectrometer setups can be used to study the influence of laser parameters on the efficiency of characteristic x-ray emission for practical applications. The advantages of the scintillator imaging system, i.e. the higher resolution and the faster read-out possibilities, will be applied in forthcoming experiments.

ACKNOWLEDGMENTS

The authors gratefully acknowledge valuable help from Ortrud Wehrhan, Ulrich Lienert (ESRF), Claes-Göran Wahlström, and Anders Persson. This work was supported by the Human Capital and Mobility Program (Contract CHRX CT93-0346), the Swedish Natural Science Research Board, the Swedish Medical Science Research Council, and personal grants from the Swedish Institute.

REFERENCES

1. J. D. Kmetec, C. L. Gordon III, J. J. Macklin, B. E. Lemoff, G. S. Brown, and S. E. Harris, *Phys. Rev. Lett.* **68**, 1527 (1992).
2. J.-C. Gauthier, J.-P. Geindre, P. Audebert, A. Rousse, A. Dos Santos, G. Grillon, A. Antonetti, and R. C. Mancini, *Phys. Rev. E* **53**, 2963 (1995).
3. K. Herrlin, G. Svahn, C. Olsson, H. Pettersson, C. Tillman, A. Persson, C-G. Wahlström, and S. Svanberg, *Radiology* **189**, 65 (1993).
4. C. L. Gordon III, G. Y. Yin, B. E. Lemoff, P. B. Bell, and C. P. J. Barty, *Opt. Lett.* **20**, 1056 (1995).
5. C. Tillman, I. Mercer, S. Svanberg, and K. Herrlin, *J. Opt. Soc. Am. B* **13**, 209 (1996).
6. P. Suortti, W. Thomlinson, D. Chapman, N. Gmür, D. P. Siddons, and C. Schulze, *Nucl. Instrum. Methods Phys. Res. A* **336**, 304 (1993).
7. G. Illing, J. Heuer, B. Reime, M. Lohmann, R. H. Menk, L. Schildwächter, W.-R. Dix, and W. Graeff, *Rev. Sci. Instrum.* **66**, 1379 (1995).
8. C. Tillman, A. Persson, C.-G. Wahlström, and S. Svanberg, in "High Field Interactions and Short Wavelength Generation," OSA Technical Digest Series Vol. 16, p. 216, Optical Society of America, Washington, DC, 1994.
9. K. Chu and A. Fenster, *Med. Phys.* **10**, 772 (1983).
10. M. Schnürer, P. V. Nickles, M. P. Kalachnikov, W. Sandner, R. Nolte, P. Ambrosi, J. L. Miquel, A. Dulieu, and A. Jolas, *J. Appl. Phys.* **80**, 5604 (1996).
11. J. Dunn, B. K. Young, A. D. Conder, and R. E. Stewart, *Proc. SPIE* **2654**, 119 (1996).
12. K. Siegbahn (Ed.), "Alpha-, Beta-, and Gamma-Ray Spectroscopy," North Holland, Amsterdam, 1965.
13. E. Förster, K. Gäbel, and I. Uschmann, *Rev. Sci. Instrum.* **63**, 5012 (1992).
14. I. Uschmann, E. Förster, H. Nishimura, K. Fujita, Y. Kato, and S. Nakai, *Rev. Sci. Instrum.* **66**, 734 (1995).
15. S. G. Pinsker, "Dynamical Scattering of X-Rays in Crystals," Springer-Verlag, Berlin, 1978.
16. D. Taupin, *Bull. Soc. Franc. Miner. Crist.* **87**, 469 (1964).
17. B. K. Tanner, "X-Ray Diffraction Topography," Pergamon, Oxford, 1976.
18. L. Dressler, F. Kafka, J. Kräusslich, and O. Wehrhan, *Crystal Res. Technol.* **25**, 1097 (1990).
19. M. Dirksmöller, O. Rancu, I. Uschmann, P. Renaudin, C. Chenais-Popovics, J. C. Gauthier, and E. Förster, *Opt. Comm.* **118**, 379 (1995).
20. J. E. White, *J. Appl. Phys.* **21**, 855 (1950).
21. M. A. Blochin, "Methoden der Röntgenspektroanalyse," Teubner, Leipzig, 1963.
22. Z. H. Kalman and S. Weissmann, *J. Appl. Crystallogr.* **16**, 295 (1983).
23. E. Erola, V. Eteläniemi, P. Suortti, P. Pattison, and W. Thomlinson, *J. Appl. Crystallogr.* **23**, 35 (1990).
24. G. Albertini, A. Boeuf, G. Cesini, S. Mazkedian, S. Melone, and F. Rustichelli, *Acta Crystallogr. A* **32**, 863 (1976).

25. J. W. Knowles, in "Alpha-, Beta-, and Gamma-Ray Spectroscopy" (S. Siegbahn, Ed.), p. 203, North Holland, Amsterdam, 1965.
26. S. Svanberg, J. Larsson, A. Persson, and C.-G. Wahlström, *Phys. Scr.* **49**, 187 (1994).
27. M. Lemonnier, R. Fourme, F. Rousseaux, and R. Kahn, *Nucl. Instrum. Methods* **152**, 173 (1978).
28. J. Miyahara, *Chem. Today* **223**, 29 (1989).
29. C. Bueno and M. D. Barker, in "X-Ray Detector Physics and Applications, San Diego, 1993," (V. J. Orphan, Ed.), SPIE Proceedings, Vol. 2009, p. 21, SPIE, Bellingham, WA, 1993.
30. J. A. Bearden, *Rev. Mod. Phys.* **31**, 125 (1967).